

Intercomparison of Bulk Microphysics Schemes in Model Simulations of Polar Lows

LONGTAO WU AND GRANT W. PETTY

Department of Atmospheric and Oceanic Sciences, University of Wisconsin—Madison, Madison, Wisconsin

(Manuscript received 30 June 2009, in final form 22 January 2010)

ABSTRACT

Four spiraliform polar lows, two over the Sea of Japan and two over the Nordic Seas, were simulated with the Weather Research and Forecasting (WRF) model. Five mixed-phase bulk microphysics schemes (BMS) provided with WRF were run respectively in order to compare their performance in polar low simulations. The observed cloud-top temperatures (CTTs) were compared with the model simulations. Precipitation rates estimated by the Advanced Microwave Scanning Radiometer for Earth Observing System (AMSR-E) and gauge-calibrated surface radar precipitation estimates around Japan were also used for validation. Although definitive validation is not possible with the available data, results from the WRF Single-Moment 6-class (WSM6) scheme appear to reproduce the cloud and precipitation processes most realistically. The model produced precipitation intensities comparable to validation products over the Sea of Japan. However, in the Nordic Seas cases, all five schemes produced significantly more precipitation than the AMSR-E estimates even though the latter estimates are known to average slightly high in the same region when validated against monthly totals measured at Jan Mayen Island (Norway).

1. Introduction

A polar low is an intense mesoscale cyclone that often develops over high latitude oceans in the cold airstreams of the polar air mass. Rasmussen and Turner (2003) define a polar low as a “small, but fairly intense maritime cyclone that forms poleward of the main baroclinic zone (the polar front or other major baroclinic zone). The horizontal scale of the polar low is approximately between 200 and 1000 kilometers and surface winds near or above gale force.” Their entire life cycles vary from several hours to several days. As polar lows are often accompanied by strong wind and heavy snowfall, they pose a potential hazard to marine traffic and operations. Because of their short life cycles, small sizes, and occurrence primarily over open ocean, they have also been notoriously difficult to study in detail using conventional surface data. With the unprecedented availability over the past decade of high-resolution satellite infrared and passive microwave observations of surface wind, precipitation, and other variables, it is now feasible to directly observe the evolution and structure of polar lows

and to assess the realism of model simulations of these storms.

In the past decades, a number of polar lows over different regions have been simulated with different numerical models. Sensitivity studies have shown that latent heat release in the convection process is crucial in order to obtain sufficient strong development of polar lows (Bresch et al. 1997; Nielsen 1997; Yanase et al. 2004; Martin and Moore 2006; Guo et al. 2007). Thus, a realistic treatment of cloud and precipitation processes is important for numerical simulation of polar lows.

A number of bulk microphysics schemes (BMS) have been developed to explicitly resolve water vapor, cloud and precipitation processes in numerical simulations (Kessler 1969; Lin et al. 1983; Rutledge and Hobbs 1983; Ziegler 1985; Meyers et al. 1997; Reisner et al. 1998). The BMS can be classified by two different methods; one is a single-moment approach and other a multiple-moment approach. The single-moment BMS predicts only the mixing ratios of the hydrometeors by representing the hydrometeor size for each class with a distribution function, such as an exponential function or a gamma type (Kessler 1969; Lin et al. 1983; Rutledge and Hobbs 1983; Ziegler 1985). Meanwhile, the double-moment BMS predicts not only the mixing ratio of the hydrometeors but also their number concentrations (Meyers et al. 1997; Reisner et al. 1998).

Corresponding author address: Grant W. Petty, Department of Atmospheric and Oceanic Sciences, University of Wisconsin—Madison, 1225 W. Dayton St., Madison, WI 53706.
E-mail: gpetty@aos.wisc.edu

To evaluate the results of different BMSs, some studies have been done on the simulations of different weather systems (Morrison and Pinto 2006; Gallus and Pfeifer 2008; Bromwich et al. 2009). For springtime Arctic mixed-phase stratiform clouds, a complex scheme was found to be better at reproducing the observed persistence and horizontal extent of the mixed-phase stratus deck (Morrison and Pinto 2006). In a German squall-line simulation, Gallus and Pfeifer (2008) evaluated the performance of the Purdue (Chen and Sun 2002), Older Thompson (Thompson et al. 2004), New Thompson (Thompson et al. 2008), WRF Single-Moment 6-class (WSM6; Hong and Lim 2006), and the WRF Single-Moment 5-class (WSM5; Hong et al. 2004) provided with the Weather Research and Forecasting (WRF) model version 2.1.2. It was found that all the five BMSs overestimate radar reflectivity in the domain, particularly in the stratiform region of the convective system. Too much graupel was produced in the schemes that included graupel as a hydrometeor. During the developing of the polar-WRF (based on the WRF version 2.2) at Byrd Polar Research Center, it was shown that the sensitivity of the WSM5, Older Thompson, and Morrison two-moment schemes (Morrison et al. 2005) was small over the western Arctic domain (Bromwich et al. 2009). However, the performance of various BMSs in representing polar low development has never been evaluated.

To evaluate the performance of different BMSs in polar low simulations, the WRF model version 3 is used to simulate four polar lows: two over the Sea of Japan and two over the Nordic Seas. Five mixed-phase BMSs were run for each case. Since all these cases have quite similar results, only the case over the Sea of Japan in December 2003 is discussed here in detail. Section 2 briefly describes the setup of the WRF simulations and datasets used in the study. The synoptic conditions for the case over the Sea of Japan in December 2003 are reviewed in section 3. In section 4, the simulation results are presented and compared with the satellite and radar observations. The final section summarizes the main conclusions.

2. Model and observational datasets

Four polar lows, two over the Sea of Japan and two over the Nordic Seas, are simulated in this study. All selected polar lows are spiraliform in shape. One representative Moderate Resolution Imaging Spectroradiometer (MODIS) image for each case is shown in Fig. 1. A summary of other key properties is listed in Table 1. Since all these cases have quite similar results, only the case over the Sea of Japan in December 2003 is discussed in detail in this paper.

a. Model description

WRF is a state-of-the-art mesoscale weather prediction system. It integrates the nonhydrostatic, compressible dynamic equations with an Arakawa C-grid using a terrain-following hydrostatic pressure vertical coordinate. The third version of the WRF model is used in this study. All our simulations were run with two nested domains at 25 km and 5 km horizontal resolution, respectively, and with 28 sigma levels in the vertical. A two-way nesting procedure is used to drive WRF with the initialization fields and boundary conditions obtained from the $1^\circ \times 1^\circ$ National Centers for Environmental Prediction final (NCEP FNL) global tropospheric analyses (more information is available online at <http://dss.ucar.edu/datasets/ds083.2/>). More details of the model setup for each case are listed in Table 2.

The principal physical schemes used in the simulations include the Yonsei University (YSU) planetary boundary layer (PBL) scheme (Hong et al. 2006), the Rapid Radiative Transfer Model (RRTM) longwave scheme (Mlawer et al. 1997, and the Dudhia (1989) shortwave scheme. A modified version of the Kain–Fritsch cumulus parameterization scheme (Kain and Fritsch 1990, 1993) is used in the outer domain. Since the convective process can be marginally resolved at 5-km resolution, no cumulus scheme is used in the inner domain as suggested by the WRF technical note (Skamarock et al. 2008). The five mixed-phase BMSs employed in the intercomparison study include the Purdue Lin (Chen and Sun 2002), the WSM6 (Hong and Lim 2006; Dudhia et al. 2008), the Goddard Cumulus Ensemble (GCE) models (Tao and Simpson 1993), New Thompson (Thompson et al. 2008), and the Morrison et al. (2009) two-moment scheme.

All these BMSs are mixed-phase schemes and include six classes of water substances: water vapor, cloud water, rain, cloud ice, snow, and graupel. The core part of the Lin scheme for representing clouds and precipitation processes is based on Lin et al. (1983) and Rutledge and Hobbs (1984). The size distribution of the rain, snow, and graupel are represented as exponential functions. The interactions among these six water substances counted in this scheme include evaporation/sublimation, deposition/condensation, aggregation, accretion, Bergeron processes, freezing, melting, and melting evaporation. Some modifications including the saturation adjustment in Tao et al. (1989) and ice sedimentation are also applied. The WSM6 scheme is similar but has the revised ice process treatment of Hong et al. (2004) and a revised terminal velocity for snow and graupel (Dudhia et al. 2008). The GCE scheme is also based on the Lin scheme, with some modifications for ice/water saturation (Tao et al. 1989, 2003).

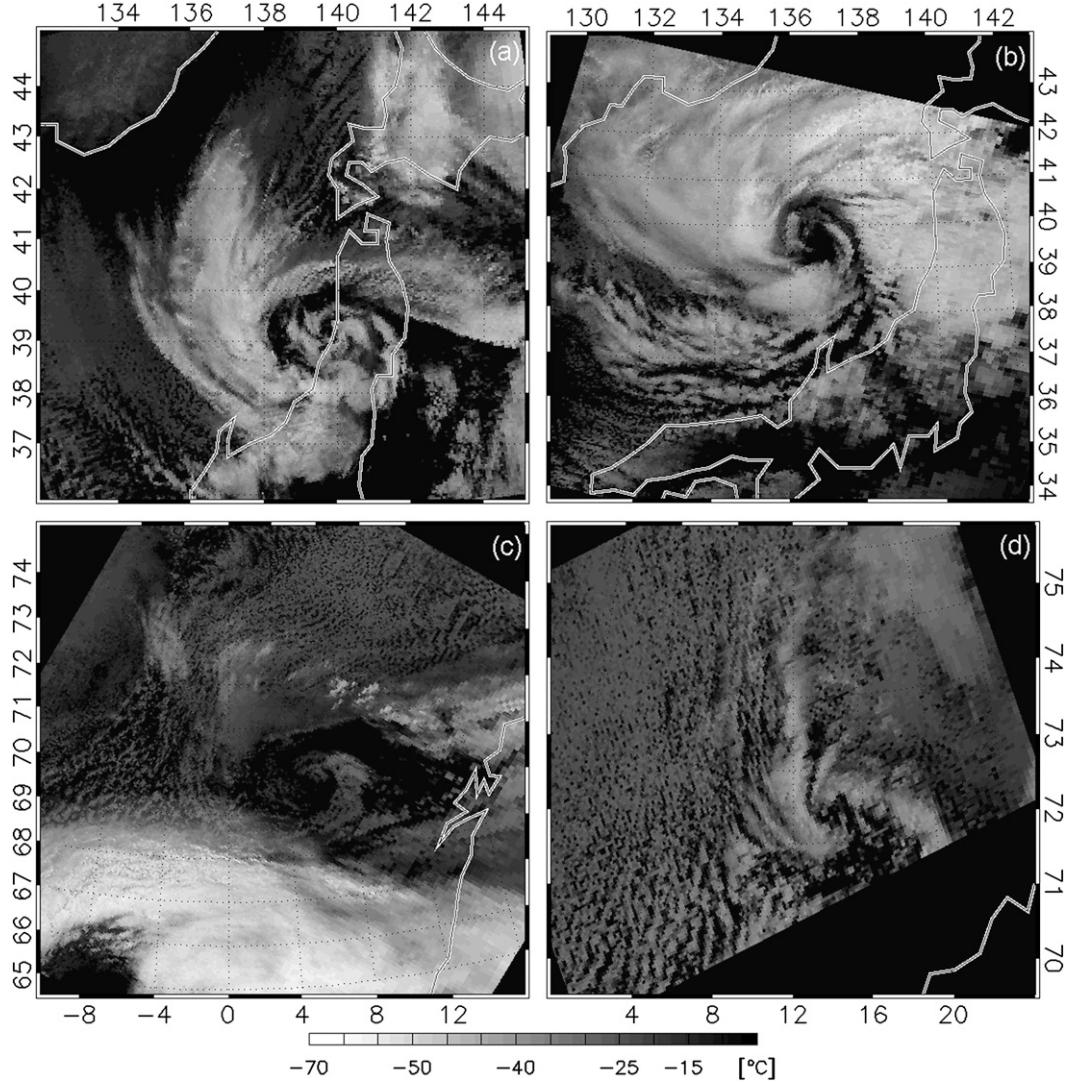


FIG. 1. MODIS CTT (channel 32) observed for the four polar low cases considered in this paper. See Table 1 for case abbreviations. (a) JP1 at 0350 UTC 20 Dec 2003, (b) JP2 at 1710 UTC 4 Dec 2005, (c) ND1 at 0325 UTC 17 Jan 2003, and (d) ND2 at 1120 UTC 5 Dec 2003.

A large number of improvements to physical parameterizations are implemented in the New Thompson scheme (Thompson et al. 2008). For example, compared to the single-moment BMSs, the New Thompson includes a two-moment prognostic scheme for cloud ice, while other single-moment components are forced to behave more like two-moment schemes. Also, snow aggregates are treated as fractal-like, with a bulk density that varies inversely with diameter. Their size distribution is represented as a sum of exponential and gamma distributions.

The Morrison et al. (2009) scheme is a two-moment scheme based on Morrison et al. (2005) and Morrison and Pinto (2006). Prognostic variables including number

concentrations and mixing ratios of the six water substances whose particle size distributions are represented as gamma functions. The size distribution intercept parameter of each hydrometeor is a specified as a function of the predicted number concentration and mixing ratio. More details of these BMSs are given by Skamarock et al. (2008).

b. AMSR-E data

The Advanced Microwave Scanning Radiometer for Earth Observing System (AMSR-E) is a multifrequency, dual-polarized microwave radiometer on board the polar-orbiting *Aqua* satellite launched in May 2002. AMSR-E is designed to retrieve column water vapor, column cloud

TABLE 1. The observation times and locations of the polar low cases. Here JP represents the cases over the Sea of Japan, ND represents the cases over the Nordic Seas, T1 means the first observation time, and T2 is the second observation time. All the times are in UTC.

Case	T1	Location	T2	Location
JP1	1645 UTC 19 Dec 2003	41.0°N, 139.0°E	0350 UTC 20 Dec 2003	39.0°N, 140.0°E
JP2	1710 UTC 4 Dec 2005	39.5°N, 137.0°E	0415 UTC 5 Dec 2005	38.5°N, 136.5°E
ND1	0145 UTC 17 Jan 2003	70.0°N, 6.0°E	0325 UTC 17 Jan 2003	70.0°N, 6.0°E
ND2	0940 UTC 5 Dec 2005	73.0°N, 14.0°E	1120 UTC 5 Dec 2003	72.5°N, 14.0°E

water, surface precipitation rate, surface wind speed, sea ice extent, sea surface temperature, and other variables (Wentz and Meissner 2007).

At mid- and high latitudes, the AMSR-E typically overpasses a given feature twice in a 24-h period. We therefore have two AMSR-E overpasses for each of the four polar low cases, and the times of these overpasses are the primary reference times for comparison with the model simulations. Overpass times are given in Table 1.

1) PRECIPITATION RETRIEVALS

The University of Wisconsin Precipitation Algorithm (UWPA) for AMSR-E is a physical inversion algorithm for retrieving precipitation rate over the ocean (Petty 1994). Physical information concerning surface precipitation rate is supplied not by the raw brightness temperatures but rather normalized polarizations for 18.7, 36.5, and 89.0 GHz (P19, P37, and P89, respectively), plus an 89.0-GHz polarization-corrected scattering index (S89), which is sensitive to scattering by ice.

The UWPA primarily relies on depolarization of ocean surface emission at lower frequencies for surface precipitation information. However when depolarization due to liquid water is either too strong or too weak to be usable, the algorithm falls back on the empirically calibrated first-guess rain rate based on S89. In this way, the dynamic range of the algorithm is extended to include both deep convection in the tropics and shallow frozen precipitation at high latitudes.

Retrieval of high-latitude ocean precipitation has historically been a major weak point of passive microwave methods (Petty 1997). Owing to the shallowness and typically light intensities characteristic of high-latitude

precipitating cloud systems, precipitation is often underestimated or overlooked completely by most published microwave algorithms. This is especially true in the absence of a rainfall at or near the surface. Although quantitative validation at high latitudes has also been difficult to access because of a lack of suitable data sources, preliminary comparisons of the UWPA estimates with monthly gauge totals at Jan Mayen Island (Norway; 70.93°N, 8.67°W) suggest that the UWPA, unlike all other algorithms we have tested, is able to retrieve reasonably unbiased monthly precipitation amounts at high latitudes, even during the cold season (Fig. 2). The same algorithm also exhibited the best overall global correlation with ship-derived climatological precipitation frequencies, as documented during the Third Precipitation Intercomparison Project (PIP-3; Adler et al. 2001). Notwithstanding the apparently good *average* performance of the UWPA for cold airmass precipitation, we cannot rule out significant over- or underestimates in specific cases. Hence, agreement or disagreement of the UWPA retrievals with the model-simulated precipitation fields can be regarded only as circumstantial evidence concerning the comparative performance of the BMSs to be taken together with other objective and subjective criteria.

2) WIND RETRIEVALS

The AMSR-E is also capable of retrieving sea surface wind speed (extrapolated to the standard 10-m reporting height) based on the influence of wind-induced roughening on the sea surface emissivity. Here we utilize the wind speed estimates included in the standard AMSR-E ocean products as described by Wentz and Meissner (2007).

TABLE 2. The details of model setup for each case. The grid size is represented by the dimension of the west–east grid by the dimension of the north–south grid. See Table 1 for case abbreviations.

	JP1	JP2	ND1	ND2
Grid size of outer domain	88 × 88	90 × 90	85 × 85	70 × 70
Center point of outer domain	38°N, 140°E	38°N, 135°E	70°N, 5°E	72°N, 18°E
Grid size of inner domain	176 × 196	201 × 201	201 × 266	151 × 151
Center point of inner domain	41.15°N, 140.29°E	39.46°N, 135.15°E	70.78°N, 2.95°E	71.66°N, 17.64°E
Initial time (UTC)	1800 UTC 18 Dec 2003	0000 UTC 4 Dec 2005	0600 UTC 16 Dec 2003	1800 UTC 4 Dec 2003
Forecast hours (h)	36	36	30	30

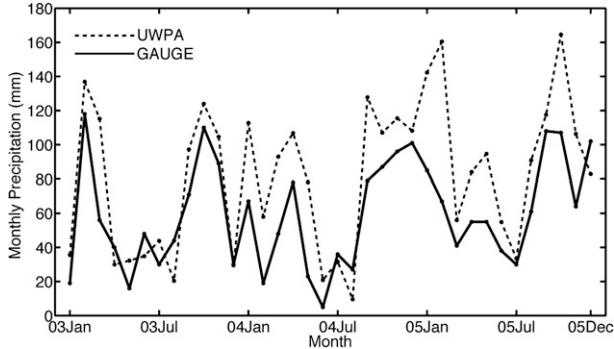


FIG. 2. UWPA estimates of monthly over-ocean precipitation (dashed line) in the vicinity of Jan Mayen Island compared with gauge totals (solid line) at the Jan Mayen meteorological station (70.93°N , 8.67°W) for 2003–05. The mean ratio (UWPA to station) is 1.38; the correlation coefficient is 0.81.

c. AMeDAS data

The Automatic Meteorological Data Acquisition System (AMeDAS) gridded precipitation dataset is a radar-based precipitation dataset covering Japan and the neighboring ocean areas. It is created from a composite of Japan Meteorological Agency (JMA) operational precipitation radars calibrated by the high-density rain gauge network over Japan (Makihara et al. 1996). It is generated by the Japan Aerospace Exploration Agency (JAXA) and is a primary tool for satellite-derived precipitation validation. We utilize a subset matched to AMSR-E overpasses of Japan and surrounding regions in 2003. The dataset covers the region between 23° – 45°N and 120° – 145°E with a spatial resolution of approximately 6 km.

For the case over the Sea of Japan in December 2003, the simulation results are compared with both the AMeDAS and UWPA products. Since there are no AMeDAS or similar data available for the other three cases, only the UWPA products are available in those cases.

d. MODIS cloud-top temperature

The MODIS (Baum and Platnick 2006) flies on the *Aqua* satellite together with the AMSR-E and provides high-resolution multichannel infrared imagery at the same times as the AMSR-E overpasses. In this study, we utilize only the cloud-top temperature (CTT) derived from the 12- μm channel in 1-km resolution for qualitative comparison with the WRF-simulated CTT.

3. Synoptic overview

At 0000 UTC 19 December 2003 a weak open low system, which later developed into a primary extratropical

cyclone, was located over northern Japan. A surface trough, which later developed into the polar low, was seen over the north of the Sea of Japan near 44°N , 140°E (Fig. 3a). Over the next 6 h, rapid development occurred as a closed low formed east of Japan with a minimum sea level pressure (SLP) of 992 hPa. To the northwest of the cyclone, the trough remained over the Sea of Japan with slight movement southwestward. The trough brought a warm moist ocean air mass to the northwest in confluence with the cold dry continental air mass. At this time a weak ridge was seen in the 1000–500-hPa thickness (Fig. 3b). By 1200 UTC 19 December, the primary extratropical cyclone continued to develop. The trough was sharper at this time, and a strong pressure gradient developed to the northwest of the trough (Fig. 3c). During the subsequent 6-h period, the primary cyclone deepened by 8 hPa to 980 hPa and moved farther southeast. The trough moved slightly southward. A closed low center with SLP minimum of 992 hPa appeared within the trough, and the pressure gradient sharpened. The ridge of the 1000–500-hPa thickness associated with the surface trough had become more intense (Fig. 3d). By 0000 UTC 20 December, the polar low had moved southeastward near 41°N , 138°E . A closed low was seen associated with the polar low but the central pressure filled by 1 hPa. The extratropical cyclone turned its movement northeastward and its low center moved out of our interest region (Fig. 3e). During the next 6-h period, the polar low continued its southeastward movement. The polar low moved over land and quickly dissipated (Fig. 3f). The entire life cycle of the polar low was less than 1 day.

Figure 1a depicts MODIS CTT at 0350 UTC 20 December. A spiraliform polar low is fully developed with a clear eye in the vortex center. Part of the polar low has moved over land. High clouds are shown west and northwest of the vortex center. To the north and northeast, a midlevel frontal cloud band separates the warm air mass from the cold air mass. Two more high cloud bands are shown over Japan: one over northern Japan and one just south of the vortex center. The extensive low-level cloud streets over the Sea of Japan reveal strong air-sea interaction there.

Figure 4a shows the AMSR-E-derived 10-m wind speed at the same time as the MODIS imagery in Fig. 1a, revealing that high speed winds nominally in excess 35 m s^{-1} exists on the southwestern flank of the polar low. It should be noted that the calibration of the microwave-derived wind speeds is uncertain at such high wind speeds.

The observational precipitation products are shown in Figs. 4c,d. The observation time for both the AMeDAS and AMSR-E products is the same as that in Fig. 1a. The

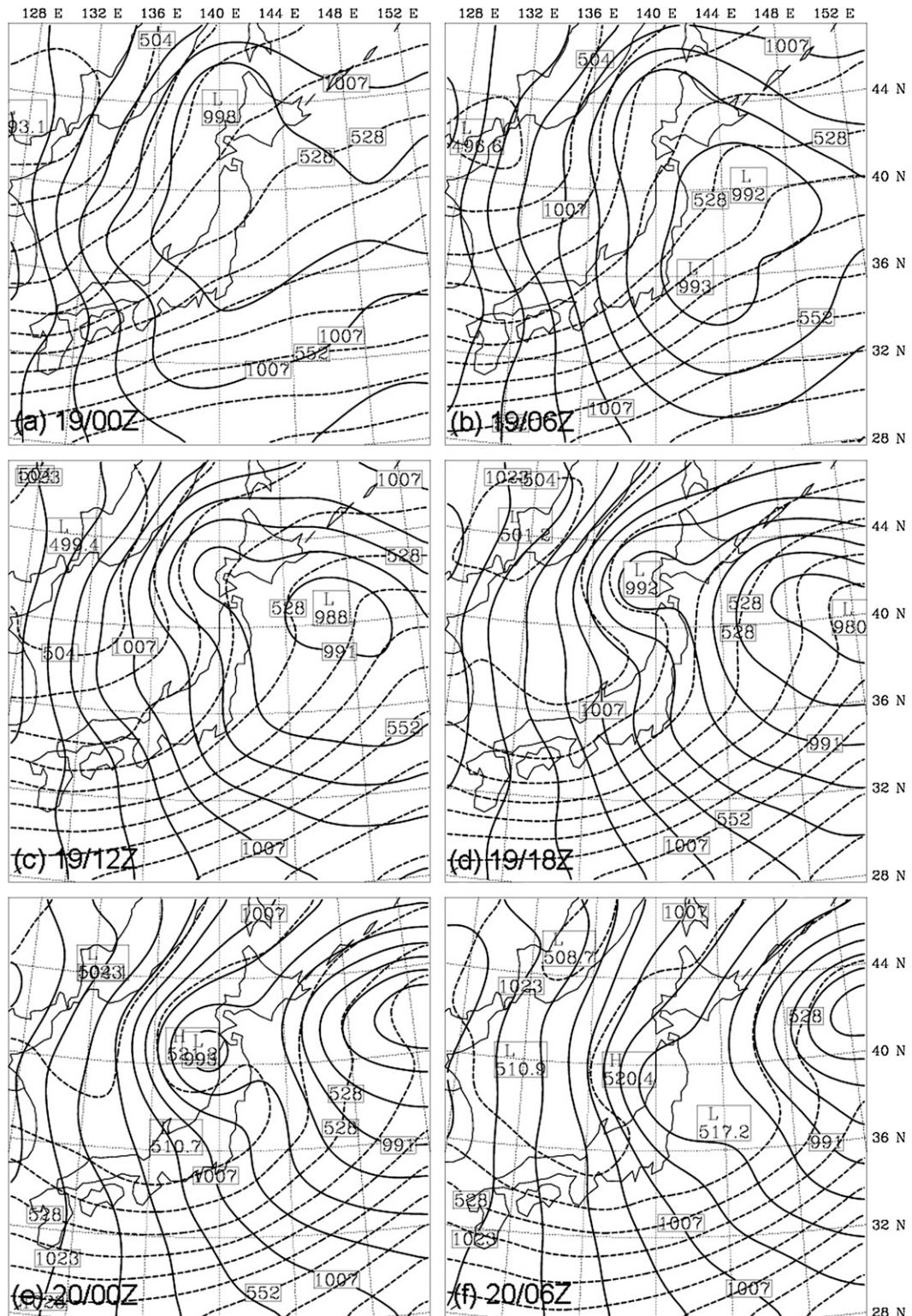


FIG. 3. NCEP FNL analyses of SLP (solid lines, contoured at 4-hPa intervals) and 1000–500-hPa thickness (dashed lines, contoured at 60-m intervals) valid at (a) 0000 UTC 19 Dec 2003, (b) 0600 UTC 19 Dec 2003, (c) 1200 UTC 19 Dec 2003, (d) 1800 UTC 19 Dec 2003, (e) 0000 UTC 20 Dec 2003 and (f) 0600 UTC 20 Dec 2003.

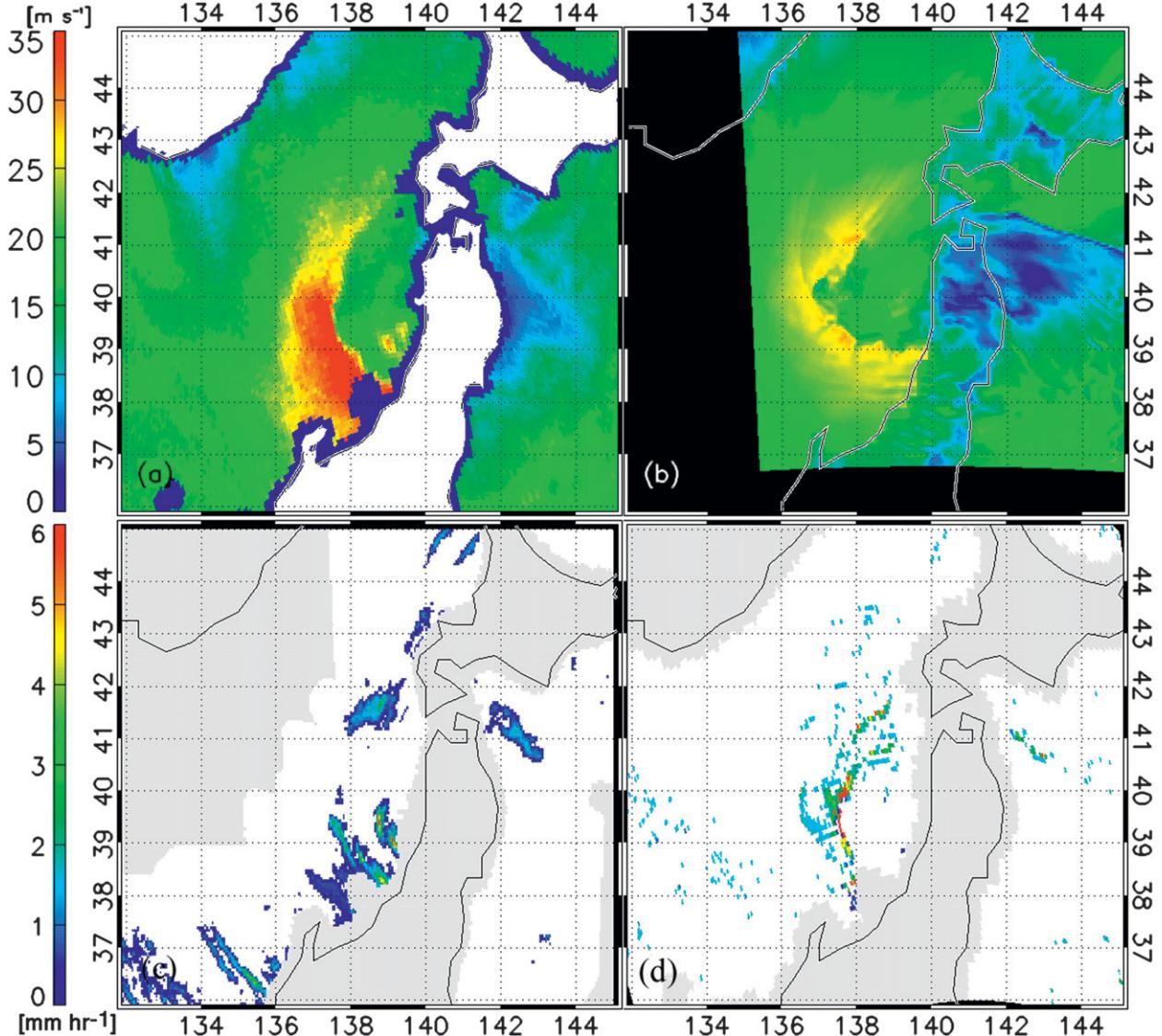


FIG. 4. Selected observations and model-simulation results at or near the AMSR-E overpass time of 0350 UTC 20 Dec 2003. (a) AMSR-E derived wind. (b) The 0400 UTC model-simulated wind speed at 5-km resolution using the WSM6 scheme. (c) The AMeDAS precipitation rate valid at 0350 UTC. (d) The UWPA precipitation rate. Gray areas in (c) and (d) indicate where no observations are possible either for the AMeDAS or UWPA products. Precipitation rates less than 0.2 mm hr^{-1} are set to white.

AMeDAS product shows that strong precipitation larger than 4 mm hr^{-1} is associated with the high clouds on the southwestern flank of the polar low. Some moderate precipitation is shown in the tail of the low. Also some light and moderate precipitation is associated with the extensive cloud streets (Fig. 4c). The UWPA product captures the main precipitation bands associated with the polar low over ocean, including one band to the west of Honshu Island and two bands at the tail of the polar low, which is located between 40° and 42°N . The coverage by precipitation is smaller while the rate is larger than that in the AMeDAS product (Fig. 4d). In the

latter, almost no precipitation is detected in the range of 40° – 41°N and 136° – 140°E . Some light-to-moderate precipitation was estimated by the UWPA algorithm there. It can be also noted that the UWPA product missed the precipitation band near the low center and some small precipitation bands close to the coast of the island. Most precipitation less than 1 mm hr^{-1} is overlooked by the UWPA product. Although these significant differences exist in the details of the AMeDAS and UWPA products, it is shown in the latter section that their domain-averaged precipitation rates are comparable.

4. Model results

a. Evaluation of the synoptic fields

To use the WRF model to evaluate the performance of BMSs in polar low simulations, it is important to show that the simulations reasonably reproduce the dynamical evolution of the polar low itself. A limited verification of the simulations is presented here. Four simulations were undertaken for polar lows developing under similar synoptic conditions, and the results for all simulations were broadly similar. The following evaluation of the synoptic fields therefore mainly focuses on one representative simulation from WSM6 at 25-km resolution.

Shown in Fig. 5 are the SLP and 1000–500-hPa thickness forecasts with 25-km resolution at 6-h intervals from 0000 UTC 19 December to 0600 UTC 20 December. The overall evolution of the simulated polar low is similar to the corresponding FNL analyses shown in Fig. 3. But a closed low developed earlier in the simulation than in the FNL analyses and with lower minimum SLP. The trajectory of the polar low is shown in Fig. 6. The position was identified when a closed low was seen over the SLP fields. At the initial stage, the simulated low was a little west of the polar low center in the analysis data. Over time, the simulated low moved to the northeast of the analyzed position.

At 0300 UTC 20 December 2003, the center of the polar low passed the weather station Akita, Japan, located at 39.72°N, 140.10°E. The location of the station is shown in Fig. 6. The station recorded a pressure drop of 7.9 hPa associated with the development of the polar low (Fig. 7a). The simulated SLP agreed very well with the observations during the first couple of forecast hours. Then a polar low started to develop earlier than the observations, and more strongly, consistent with Fig. 5. The minimum SLP passed Akita 1 h later than in the simulation. The observations at Aikawa, which is a small island in the Sea of Japan, show the same trend but with smaller difference between observations and simulations (Fig. 7c).

The 5 km-resolution simulated wind speed field at 0400 UTC 20 December is presented in Fig. 4b. The maximum wind speed of 28 m s^{-1} is smaller than the AMSR-E wind product in Fig. 4a. The large-scale wind pattern generally agrees with the AMSR-E wind product but with more finescale structures produced by the simulation. At Aikawa, the highest wind speed of 29 m s^{-1} was recorded at 0400 and 0500 UTC 20 December. For most of the time period, the modeled wind speed matched up well with the observed one (Fig. 7d). However, a peak of high wind speed up to 24 m s^{-1} was shown in the simulation while no high wind speeds were recorded at Akita (Fig. 7b). This is because the center of the

simulated polar low passed approximately 100 km northeast of the analyzed center.

Figure 8 shows the sounding data at Akita. At 1200 UTC 19 December 2003, the profiles of temperature and dew-point temperature match up very well between the simulation and observation except that the dewpoint temperature is a little lower in the simulation (Fig. 8a). Above the 900-hPa level, the profiles still show reasonable agreement at 0000 UTC 20 December (Fig. 8b). However, below that layer, the simulated temperatures are several degrees higher than the observations. The observed surface temperature was approximately 0°C while the simulated temperature is $\sim 6^\circ\text{C}$.

Given the overall consistency, we can have some confidence in using the WRF simulations in our investigation of the effect of different BMSs on polar low simulations.

b. Cloud-top temperature

Figure 9 displays the 5-km resolution CTTs from the five BMSs valid at 0400 UTC 20 December 2003. For all these five BMSs, the location of the low center is a little farther north than the observation and the orientation of the polar low shows more of counterclockwise rotation. However the relative position of the polar low between these simulations is almost consistent. It reveals that different BMS do not significantly influence the propagation of the low system.

The BMS choice does, however, strongly affect the simulated CTT. For example, in the Lin scheme (Fig. 9b), the northern flank of the polar low is almost entirely covered by high clouds with similar CTT. The WSM6 (Fig. 9c) produced reasonable extent and structure of the cloud shield. High clouds are associated with the polar low and low clouds correspond to cloud streets. The shape of the cloud shields in the GCE scheme is similar with the WSM6. But there are fewer high clouds, and the high clouds have a looser structure (Fig. 9d). For the New Thompson scheme (Fig. 9e), almost no high clouds were produced corresponding to the polar low. The Morrison two-moment scheme (Fig. 9f) has more high-cloud coverage. Overall, the Lin and New Thompson did poorly in producing cloud fields while the cloud fields in other three schemes seem fairly realistic.

c. Precipitation

The simulated precipitation rates at 5-km resolution are shown in Fig. 10 as generated by the explicit micro-physics scheme; no cumulus parameterization was used in the inner domain. All five experiments successfully reproduced the main pattern of the precipitation associated with the polar low. The precipitation associated with the cloud streets and the precipitation over land are also depicted in the simulations. Comparing the five

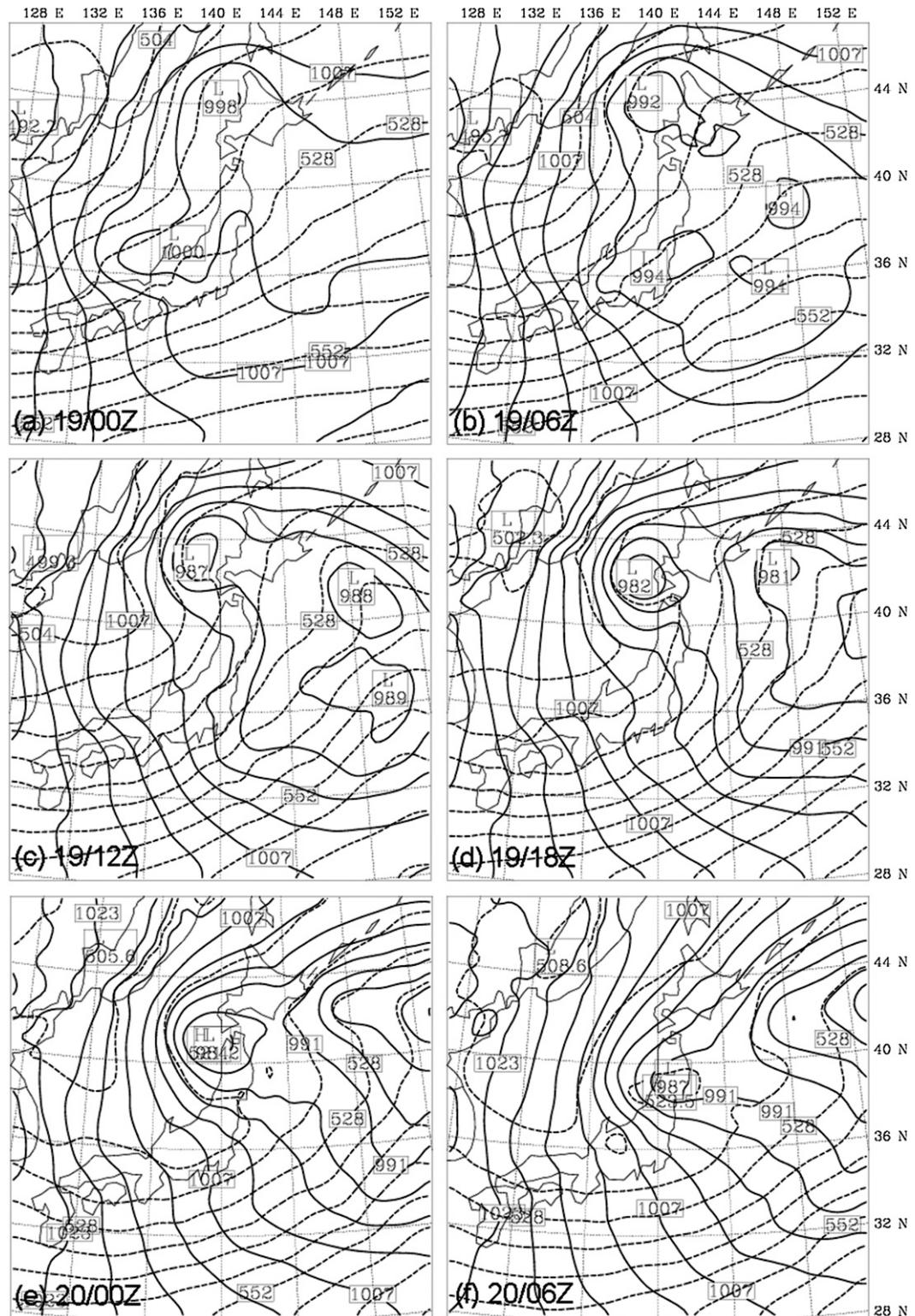


FIG. 5. WRF forecast of SLP (solid lines) and 1000–500-hPa thickness (dashed lines) (a) 6-h forecast valid at 0000 UTC 19 Dec 2003, (b) 12-h forecast valid at 0600 UTC 19 Dec 2003, (c) 18-h forecast valid at 1200 UTC 19 Dec 2003, (d) 24-h forecast valid at 1800 UTC 19 Dec 2003, (e) 30-h forecast valid at 0000 UTC 20 Dec 2003, and (f) 36-h forecast valid at 0600 UTC 20 Dec 2003.

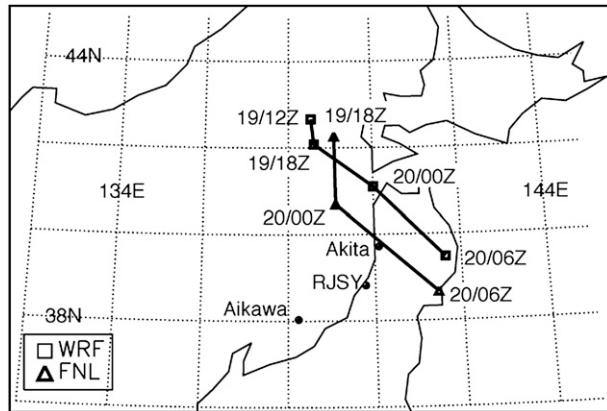


FIG. 6. The trajectory of polar low center as obtained from the WRF simulation at 25-km resolution (squares) and the FNL analyzed data (triangles) with 6-h intervals. The position was identified when a closed low was seen over the SLP fields. The FNL analyses are from 1800 UTC 19 Dec 2003 to 0600 UTC 20 Dec 2003. The WRF simulations are from 1200 UTC 19 Dec 2003 to 0600 UTC 20 Dec 2003.

simulations, both the Lin and WSM6 schemes show precipitation rates greater than 4 mm h^{-1} while in others the maximum rate is smaller. More complex precipitation structures are depicted in the Lin scheme (Fig. 10a). The precipitation pattern is smoother in the GCE scheme (Fig. 10c).

To illustrate the three-dimensional structure of the simulated water substances, Fig. 11 depicts the vertical profiles of domain-averaged water content for each hydrometeor (leftmost column) and the column-integrated water content for cloud water, cloud ice, snow and graupel (remaining columns). The domain-averaged water content is only calculated over a box that encompasses the precipitation associated with the polar low. All of these schemes show light rainfall near the surface, and column-integrated rainwater is fairly similar for all five schemes (not shown), which is consistent with the station observations of showers of mixed rain and snow and with surface air temperatures only $1\text{--}3^\circ\text{C}$ above freezing. Column-integrated water vapor (not shown) is fairly similar among all five schemes, but dissimilar from AMSR-E-observed product (Wentz and Meissner 2007) in having considerably more finescale structure but less area covered by low values.

For the Lin scheme (Fig. 11a), the primary hydrometeor type from 950 to 500 hPa is graupel, in sharp contrast to all four other schemes. The maximum domain-averaged graupel content appears around 900 hPa with a value close to 0.12 g m^{-3} . It produced widespread graupel in the lowest layers, even in stratiform areas. Very little column-integrated snow is predicted. What little snow is present is mainly found at high levels in the clouds, and

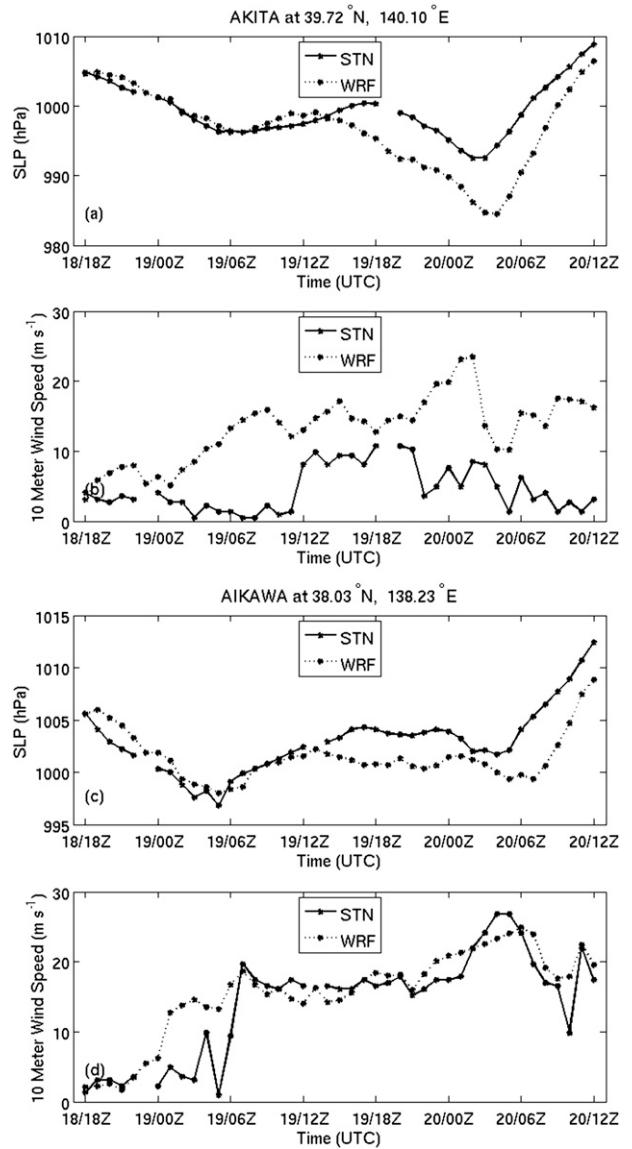


FIG. 7. Time series of modeled (dashed) and station-observed (solid line) SLP and wind speed at Akita (39.71°N , 140.10°E) and Aikawa (38.03°N , 138.23°E). (a) Akita SLP, (b) Akita wind speed, (c) Aikawa SLP, and (d) Aikawa wind speed.

little or no snow is found in the lowest layer. The widespread graupel may be related to the parameterization of the terminal velocity for snow and graupel, which was subsequently modified in WSM6 with an aim to achieving more reduced conversion rates from snow to graupel (Dudhia et al. 2008).

In WSM6 (Fig. 11b), the largest part of the hydrometeor content is snow, but the amount is less than produced by GCE, New Thompson, and Morrison. Graupel appears as a close second and is confined mainly to stronger convective cells and bands, as expected. The least column-integrated cloud water is predicted by WSM6

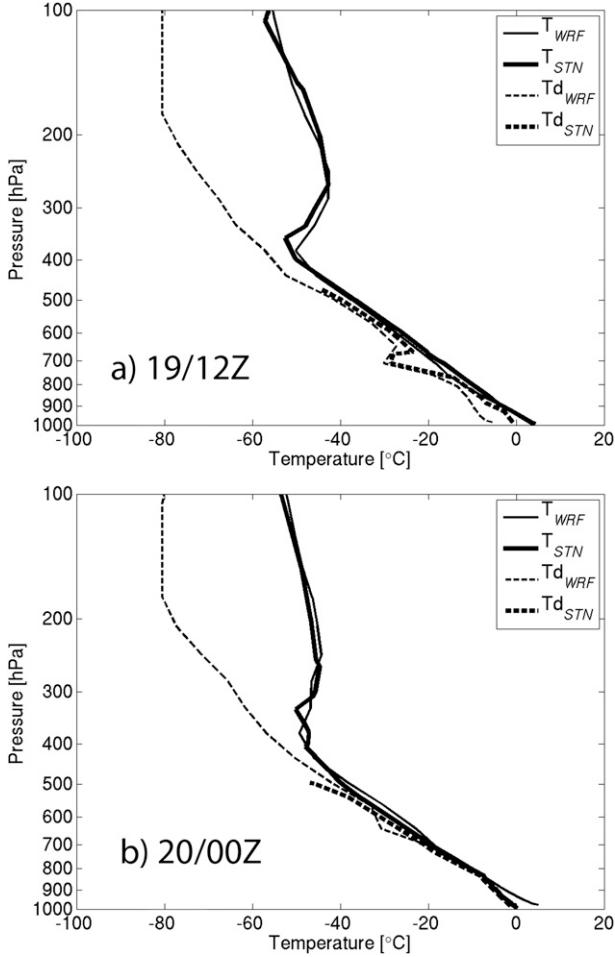


FIG. 8. Observed (thin lines) and simulated (thick lines) atmospheric temperature (solid) and dewpoint (dashed) profiles at Akita valid at (a) 1200 UTC 19 Dec 2003 and (b) 0000 UTC 20 Dec 2003.

while the same scheme produces heavy cloud ice down to unexpectedly low levels, suggesting that clouds glaciate very easily in this scheme. Relative to the Lin scheme, a substantially revised approach for ice microphysical processes was provided by Hong et al. (2004) with the intent of producing more realistic cloud ice (Dudhia et al. 2008; Hong and Lim 2006; Hong et al. 2004). However, while the revised formulations indeed reduced initial ice nuclei concentration and ice amounts significantly at very cold temperatures, they sharply *increased* these quantities at temperatures between 0° and -20°C as shown, for example, in Fig. 2a of Hong et al. (2004). We surmise that the modeled cloud ice concentrations at low altitudes are an unintended side effect of these changes.

Using the GCE scheme (Fig. 11c), the whole domain is dominated by snow with the maximum local snow content up to 4.50 g m^{-3} at 870 hPa. Graupel mainly appears

within stronger precipitation bands. Moderate cloud water and ice are also shown in the GCE scheme.

The New Thompson scheme (Fig. 11d) is unique in producing essentially no cloud ice or graupel whatsoever, even in convective cells and bands. Snow dominates in the whole profile with two peaks at 875 and 500 hPa, respectively. The large amount of snow in the New Thompson scheme may be due to their snow particle size distribution function. The scheme utilizes a sum of exponential and gamma functions that produces more numerous small snow particles, which in turn reduces sedimentation and increases vapor deposition (Thompson et al. 2008).

The Morrison two-moment scheme (Fig. 11e) predicted the most column-integrated cloud water and the largest domain-averaged cloud water in the lower layers. Mainly in the convective bands and cells, substantial cloud water up to 1 g m^{-3} is produced in the lowest model layer (not shown), which includes the atmospheric layer from the surface to roughly 28 m above the surface. Such high cloud water in the lowest model layer seems unphysical, especially since the synoptic environment did not favor fog formation. The association of low-level cloud water with convective bands might be related to more efficient evaporation of rainfall below the cloud base in convective environments (Morrison et al. 2009) owing to a higher raindrop size distribution intercept parameter associated with convective rain and, therefore, a proliferation of smaller raindrops. However, it remains difficult to understand how accelerated evaporation of rainwater could be physically consistent, in the same environment, with accelerated formation of cloud water consisting of even smaller droplets.

At 0200 UTC 20 December 2003, moderate-to-heavy showers of snow pellets or small hail [World Meteorological Organization (WMO) present weather code 88] was reported by ship “RJSY” (location shown in Fig. 6), “snow pellets” being the common term for graupel reaching the surface. Also during the 5-yr project, the Cooperative Japan Sea Snow Cloud Project (Murakami et al. 1994, 2003), a mixture of graupel and snow was observed in the convective snow clouds over the Sea of Japan. Supercooled water and ice also existed in the developing and mature stage of the snow clouds. In the mature stage, a large amount of the supercooled water was depleted by snow and graupel (Murakami et al. 1994, 2003). Overall, the Lin and New Thompson scheme seem to have problem in producing snow or graupel in the environment for polar low development. It may explain their poor performance in producing realistic cloud fields. The other three schemes successfully produced a mixture of supercooled water, cloud ice, snow, and graupel. However, we question the tendency of WSM6

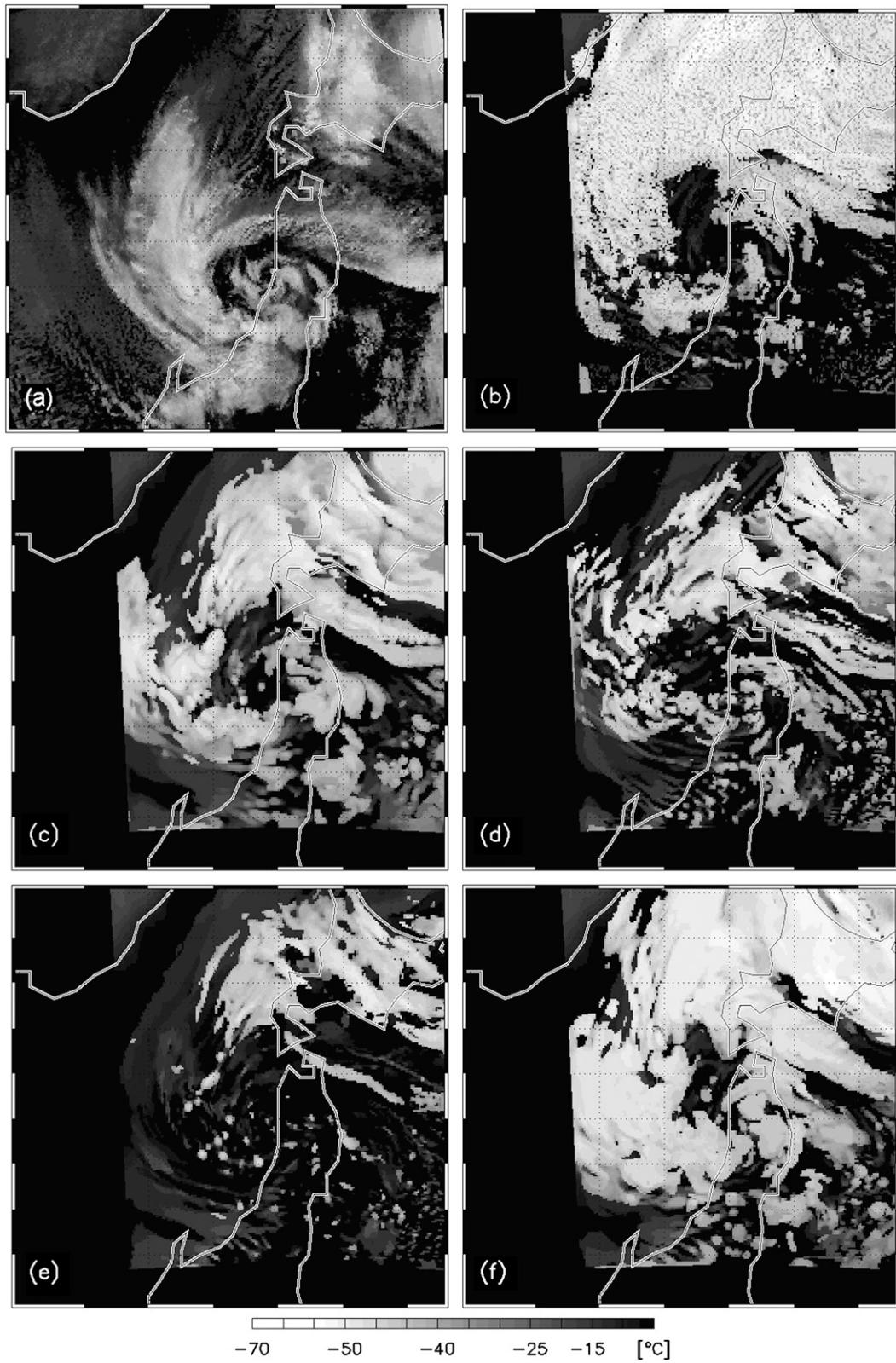


FIG. 9. Simulated CTT at 5-km resolution for (b) Lin, (c) WSM6, (d) GCE, (e) New Thompson, and (f) Morrison two-moment schemes. Valid at 0400 UTC 20 Dec 2003. The MODIS CTT is shown in (a) for comparison.

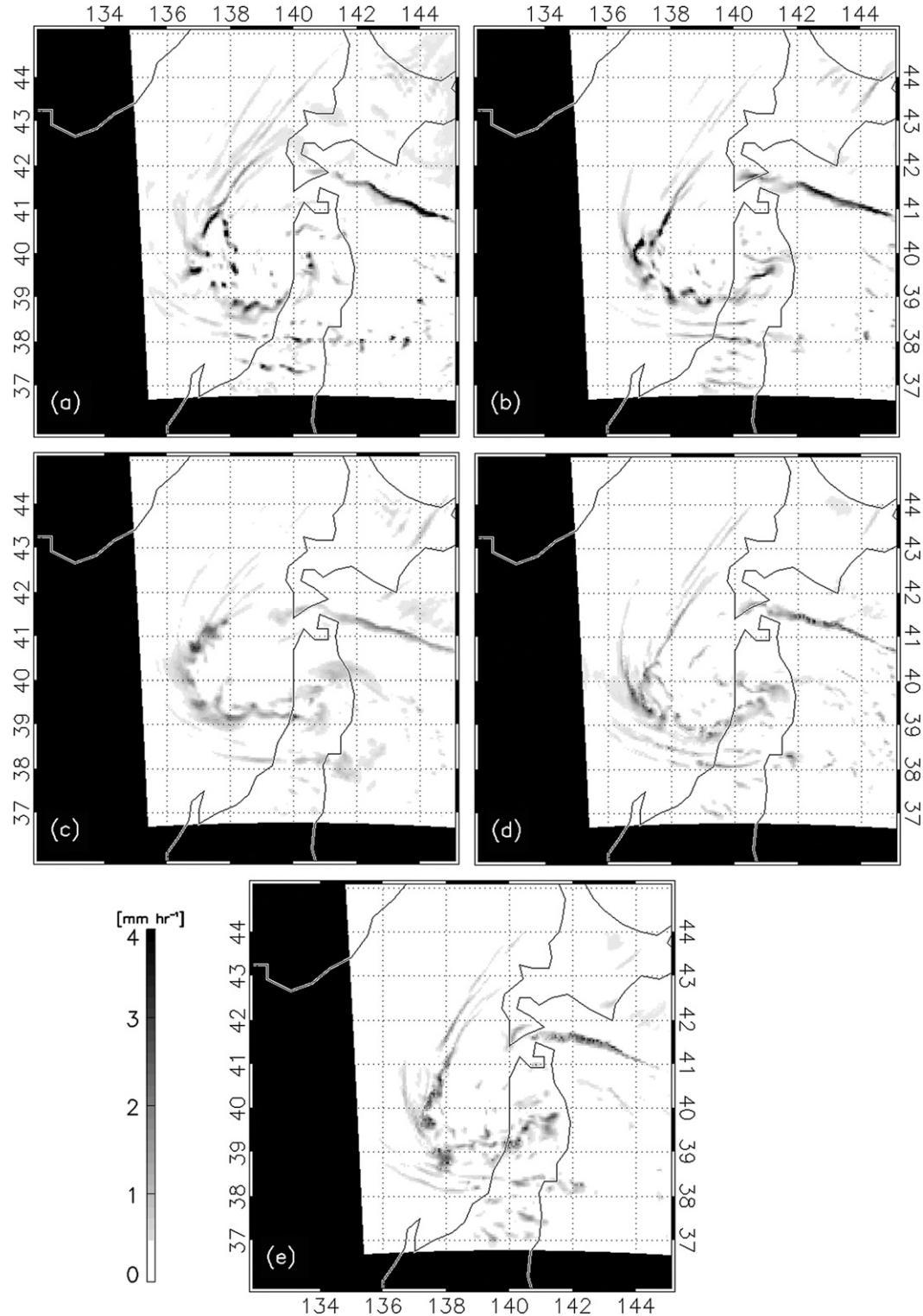


FIG. 10. The simulated precipitation rate at 5-km resolution for (a) Lin, (b) WSM6, (c) GCE, (d) New Thompson, and (e) Morrison two-moment schemes. Valid at 0400 UTC 20 Dec 2003.

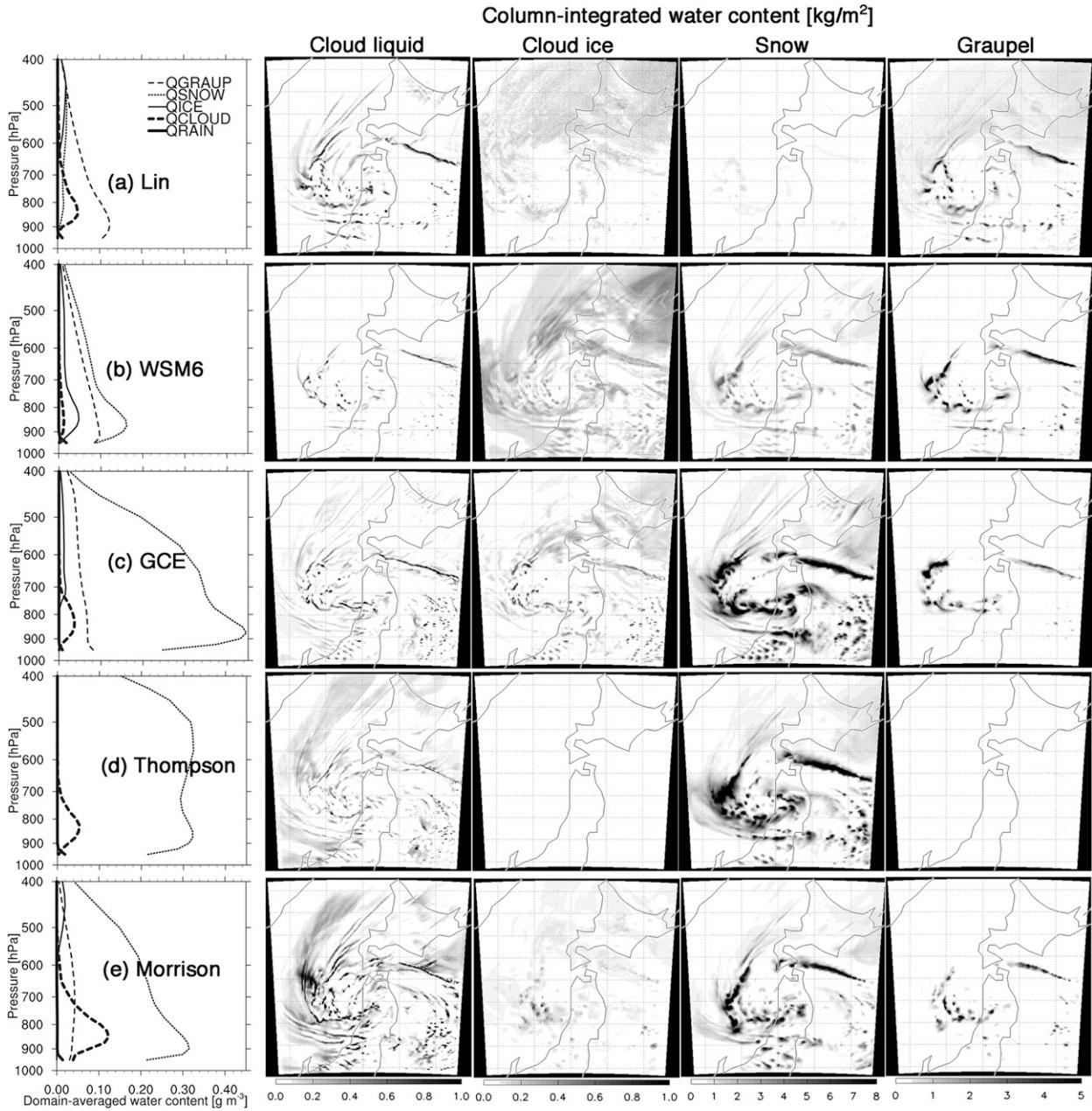


FIG. 11. The distribution of water contents at 0400 UTC 20 Dec 2003 for (a) Lin, (b) WSM6, (c) GCE, (d) New Thompson, and (e) Morrison two-moment schemes. The first column (column 1) is the vertical distribution of the domain-averaged water contents for cloud water (QCLOUD), cloud ice (QICE), snow (QSNOW), rain (QRAIN), and graupel (QGRAUP). Subsequent columns are the column-integrated water content (kg m^{-2}) for (column 2) cloud liquid water, (column 3) cloud ice, (column 4) snow, and (column 5) graupel.

to produce widespread cloud ice in the lower layers, likewise the tendency of Morrison to produce heavy cloud liquid water at very low altitudes.

In summary, our examination of hydrometeor concentrations yields the following assessments:

- Lin: Produces almost no snow. Graupel seems too widespread, especially in stratiform clouds.

- WSM6: Produces the least cloud liquid water and probably too much cloud ice down to low elevations. This suggests that supercooled clouds may glaciate too readily. It also produces the second-lowest snow content.
- GCE: Heaviest snow concentration; other fields seem plausible.
- Thompson: No cloud ice or graupel at any level, heavy snow concentrations over deep layer.

TABLE 3. The maximum spatial correlation between WRF simulation and observations of precipitation patterns at 20-km resolution. Boldface values are the maximum values achieved for a particular comparison time. See Table 1 for case abbreviations.

Case	Time	Validation data	BMS				
			Lin	WSM6	GCE	Thompson	Morrison
JP1	T1	UWPA	0.07	0.10	0.09	0.10	0.13
		AMeDAS	0.23	0.27	0.19	0.23	0.17
	T2	UWPA	0.45	0.68	0.60	0.66	0.65
		AMeDAS	0.28	0.48	0.34	0.46	0.46
JP2	T1	UWPA	0.55	0.63	0.48	0.56	0.54
	T2	UWPA	0.33	0.38	0.38	0.34	0.29
ND1	T1	UWPA	0.54	0.46	0.49	0.57	0.48
	T2	UWPA	0.10	0.25	0.19	0.22	0.08
ND2	T1	UWPA	0.54	0.51	0.62	0.61	0.59
	T2	UWPA	0.54	0.44	0.34	0.48	0.43
Combined			0.37	0.43	0.37	0.40	0.38

- Morrison: Anomalously large cloud water contents, including in lowest model layer.

d. Statistical comparisons

1) SPATIAL CORRELATIONS

An additional test we undertook was the evaluation of the spatial patterns of precipitation produced by the five BMSs. For the case over the Sea of Japan in December 2003, the simulation results are compared with both the AMeDAS and UWPA products. Since there are no AMeDAS or similar data available for the other three cases, only the UWPA products are used for validation in those cases. We computed spatial correlation coefficients between the observed (UWPA and/or AMeDAS) precipitation fields and the modeled fields. For these calculations, the observations were projected onto the model grid, which is at 5-km resolution. Any point without data (UWPA or AMeDAS products) was set to zero in both fields being compared. Then both the observed and simulated fields were smoothed by averaging with a 4×4 window to a resolution of 20 km.

To account for spatial displacement between the observed and simulated polar low center, we shifted the fields relative to one another and recorded the maximum correlation achieved for any horizontal displacement, following common practice in pattern-matching algorithms (Haralick and Shapiro 1992; Lewis 2003).

These spatial correlations were obtained for four polar lows, two AMSR-E overpass times each, and five BMSs. In addition, correlations with AMeDAS results are available for the two overpass times associated with the first polar low case over the Sea of Japan. Results are given in Table 3. It can be seen that most of the cases show good agreement with the observations, with maximum correlations up to 0.68. In more than half of the cases, the WSM6 scheme shows the best spatial similarity with

the observations. Combining all the cases together, the WSM6 scheme presents the maximum correlation of 0.43.

2) DOMAIN-AVERAGED PRECIPITATION

The domain-averaged precipitation rate over the region with the maximum correlation is also calculated and compared with the observations (Table 4). As noted in section 3, the UWPA product estimates stronger precipitation rates in the strong precipitation band and overlooks the lightest precipitation. However, the domain-averaged precipitation rates are comparable. At 1645 UTC 19 December 2003 in the first case over the Sea of Japan, UWPA has a mean value 0.29 mm h^{-1} while AMeDAS is 0.16 mm h^{-1} . At the second observation time, UWPA has a mean value 0.32 mm h^{-1} while AMeDAS is 0.17 mm h^{-1} . Although the averaged precipitation rate is still higher in UWPA, a factor of 1.9 is acceptable in view of the inherent uncertainties associated with passive microwave precipitation retrievals in cold environments.

Over the Sea of Japan, the domain-averaged precipitation rates in the observations are of the order of 0.1 mm h^{-1} (Table 4). The ratio of simulation to observation ranges from 0.4 to 1.5. The simulations are thus not inconsistent with the observations when one allows for about a factor of 2 uncertainty in the latter.

However, over the Nordic Seas, the observed domain-averaged precipitation rates are of the order of 0.01 mm h^{-1} , which is considerably below that produced by the simulations. Especially for the second Nordic Seas case at 1120 UTC 5 December 2003, the ratio of all the simulations to the UWPA is greater than 5. In all these cases, the Lin scheme predicted the largest averaged precipitation rate. In most cases, the WSM6 gives the second-largest amount. The other three schemes had similar but slightly lower values in most of the cases. Note that both polar low cases occurred within $\sim 1^\circ$ latitude of Jan Mayen Island, where our 3-yr comparison of UWPA

TABLE 4. Ratios of domain-averaged precipitation rates derived from the WRF simulations to the indicated validation data source (rightmost column). See Table 1 for case abbreviations.

Case	Time	Validation data	Ratio of BMS results to obs					Obs (mm hr ⁻¹)
			Lin	WSM6	GCE	Thompson	Morrison	
JP1	T1	UWPA	0.60	0.46	0.44	0.45	0.45	0.29
		AMeDAS	1.10	0.85	0.76	0.80	0.80	0.16
	T2	UWPA	0.88	0.72	0.65	0.62	0.65	0.32
		AMeDAS	1.41	1.06	0.84	0.95	0.98	0.17
JP2	T1	UWPA	0.73	0.58	0.58	0.56	0.55	0.38
	T2	UWPA	0.76	0.56	0.53	0.51	0.53	0.32
ND1	T1	UWPA	6.82	4.12	3.93	4.00	3.97	0.02
	T2	UWPA	2.45	2.06	2.08	2.06	1.95	0.03
ND2	T1	UWPA	2.63	2.43	1.58	1.96	2.13	0.04
	T2	UWPA	7.76	7.07	5.29	7.10	6.98	0.01

estimates with gauge amounts (Fig. 2) revealed a modest *overestimate* of monthly totals by the satellite product. It therefore cannot simply be assumed that the UWPA was biased low by a factor of 5 in these particular cases, though it also cannot be ruled out.

5. Summary and discussion

In this study, we investigated the influence of five mixed-phase BMSs on simulations of four spiraliform polar lows. The purpose was to identify the BMS that is likely to be most suitable for subsequent model-based investigations of the role of moist processes in the dynamics of polar low development.

It was found that the choice of BMS did not have much effect on the location of the polar low development. However, the simulated CTT and precipitation fields were quite different. It is our assessment that the Lin and New Thompson schemes did not yield cloud fields that were qualitatively consistent with the observed CTT.

The primary hydrometeor in the Lin scheme is graupel while snow is the predominant component in the other BMSs. Consistent with a local ship weather report as well as in situ field observations of convective snow clouds over the Sea of Japan (Murakami et al. 1994, 2003), mixed snow and graupel with small amount of super cooled water were predicted in the WSM6, GCE, and Morrison two-moment schemes. Based on the maximum correlation between the modeled and observed precipitation rates, all simulations were deemed to produce fairly reasonable spatial patterns of precipitation, though the details clearly differed from one scheme to the next. Overall, the WSM6 scheme yielded the best overall spatial/temporal correlation with the observed precipitation fields.

The domain-averaged precipitation rates were computed around the regions of polar lows. It was shown that the Lin scheme consistently has the largest average

precipitation rate. The WSM6 scheme is the second-largest in most of the cases while other BMSs produced lighter precipitation. The observed precipitation over the Sea of Japan is an order of magnitude higher than those over the Nordic Seas. Over the Sea of Japan, the WRF model produced precipitation intensities comparable to the observations. However, over the Nordic Seas, much higher precipitation rates were modeled than were estimated via satellite, especially at the time that only very light precipitation was observed. While it is known that microwave retrievals can have difficulty detecting high-latitude precipitation, the UWPA product is notable for slightly overestimating monthly surface gauge totals at the same latitude throughout most of the 3-yr period 2003–05 (Fig. 2).

The difference in apparent model performance between the Sea of Japan and Nordic Seas could be because of three reasons. First, the UWPA product is likely to overlook the lightest precipitation. Over the Nordic Seas, it is colder and less moist than over the Sea of Japan. Also the two cases over Nordic Seas are shallower than the cases over Sea of Japan. Most of the precipitation intensity is smaller than 2 mm h^{-1} , which may be below the detection threshold of the UWPA algorithm when precipitation reaches the surface as snow. If very little precipitation occurred at higher rates, then the UWPA would not detect the majority of the total precipitation that fell. Second, the initialization data over the Nordic Seas may be less reliable on account of the sparseness of surface data. The third reason may be that the BMSs simply do not simulate this kind of cold shallow precipitation well at high latitudes.

Table 5 summarizes our comparison results. The WSM6 scheme showed reasonable results for CTT, maximum precipitation, and spatial correlation. It also produced plausible combinations of cloud water, cloud ice, snow, and graupel. But there might be some question concerning

TABLE 5. Summary of assessments. A check (✓) indicates “satisfactory” performance, with caveats noted where applicable.

	CTT	Max precipitation rate	Best precipitation spatial correlation	Hydrometeor fields
Lin		✓		
WSM6	✓	✓	✓	✓ (too much cloud ice?)
GCE	✓			✓
Thompson				
Morrison	✓			✓ (too much cloud liquid water?)

its production of widespread cloud ice in the lower layers. Notwithstanding the unavoidable ambiguities, our assessment based on both subjective and objective criteria is that the WSM6 scheme is marginally superior to the others in reproducing cloud and precipitation processes overall. High-quality surface and in situ aircraft cloud physical measurements would be required in order to give greater confidence to this finding. Unfortunately, such data are not readily available over the regions where most polar lows form.

Acknowledgments. The authors thank to Dr. Gunnar Noer and Dr. Wataru Yanase for sharing their compilation of polar low cases. The authors also thank Professor Jonathan Martin for valuable discussions. Thanks also to Mr. Pete Pokrandt, Mr. Yunfei Zhang, and the WRF support staff for their assistance with setting up the WRF simulations. The comments of two anonymous reviewers are also appreciated. The AMSR-E L2 data and AMeDAS match-up data were obtained from the Japan Aerospace Exploration Agency (JAXA) Earth Observation Research Center (EORC). This study was supported by NASA Grant NNX08AD36G.

REFERENCES

- Adler, R. F., C. Kidd, G. Petty, M. Morissey, and H. M. Goodman, 2001: Intercomparison of global precipitation products: The Third Precipitation Intercomparison Project (PIP-3). *Bull. Amer. Meteor. Soc.*, **82**, 1377–1396.
- Baum, B. A., and S. Platnick, 2006: Introduction to MODIS cloud products. *Earth Science Satellite Remote Sensing, Vol. 1: Science and Instruments*, J. J. Qu et al., Eds., Tsinghua University Press and Springer-Verlag, 74–91.
- Bresch, J. F., R. J. Reed, and M. D. Albright, 1997: A polar-low development over the Bering Sea: Analysis, numerical simulation, and sensitivity experiments. *Mon. Wea. Rev.*, **125**, 3109–3130.
- Bromwich, D. H., K. M. Hines, and L.-S. Bai, 2009: Development and testing of polar weather research and forecasting model: 2. Arctic Ocean. *J. Geophys. Res.*, **114**, D08122, doi:10.1029/2008JD010300.
- Chen, S.-H., and W.-Y. Sun, 2002: A one-dimensional time dependent cloud model. *J. Meteor. Soc. Japan*, **80**, 99–118.
- Dudhia, J., 1989: Numerical study of convection observed during the winter monsoon experiment using a mesoscale two-dimensional model. *J. Atmos. Sci.*, **46**, 3077–3107.
- , S.-Y. Hong, and K.-S. Lim, 2008: A new method for representing mixed-phase particle fall speeds in bulk microphysics parameterizations. *J. Meteor. Soc. Japan*, **86A**, 33–44.
- Gallus, W. A., Jr., and M. Pfeifer, 2008: Intercomparison of simulations using 5 WRF microphysical schemes with dual-polarization data for a German squall line. *Adv. Geosci.*, **16**, 109–116.
- Guo, J. T., G. Fu, Z. L. Li, L. M. Shao, Y. H. Duan, and J. G. Wang, 2007: Analyses and numerical modeling of a polar low over the Japan Sea on 19 December 2003. *Atmos. Res.*, **85** (3–4), 395–412.
- Haralick, R. M., and L. G. Shapiro, 1992: *Computer and Robot Vision*. Vol. II. Addison-Wesley, 630 pp.
- Hong, S.-Y., and J.-O. J. Lim, 2006: The WRF Single-Moment 6-Class Microphysics Scheme (WSM6). *J. Korean Meteor. Soc.*, **42**, 129–151.
- , J. Dudhia, and S.-H. Chen, 2004: A revised approach to ice microphysical processes for the bulk parameterization of clouds and precipitation. *Mon. Wea. Rev.*, **132**, 103–120.
- , Y. Noh, and J. Dudhia, 2006: A new vertical diffusion package with an explicit treatment of entrainment processes. *Mon. Wea. Rev.*, **134**, 2318–2341.
- Kain, J. S., and J. M. Fritsch, 1990: A one-dimensional entraining/detraining plume model and its application in convective parameterization. *J. Atmos. Sci.*, **47**, 2784–2802.
- , and —, 1993: Convective parameterization for mesoscale models: The Kain-Fritsch scheme. *The Representation of Cumulus Convection in Numerical Models*, Meteor. Monogr., No. 46, Amer. Meteor. Soc., 165–170.
- Kessler, E., 1969: *On the Distribution and Continuity of Water Substance in Atmospheric Circulations*. Meteor. Monogr., No. 32, Amer. Meteor. Soc., 84 pp.
- Lewis, J. P., cited 2003: Fast normalized cross-correlation. [Available online at <http://www.idiom.com/~zilla/Papers/nvisionInterface/nip.html>.]
- Lin, Y.-L., R. D. Farley, and H. D. Orville, 1983: Bulk parameterization of the snow field in a cloud model. *J. Climate Appl. Meteor.*, **22**, 1065–1092.
- Makihara, Y., N. Uekiyo, A. Tabata, and Y. Abe, 1996: Accuracy of Radar-AMeDAS precipitation. *IEICE Trans. Commun. E*, **79-B**, 751–762.
- Martin, R., and G. W. Moore, 2006: Transition of a synoptic system to a polar low via interaction with the orography of Greenland. *Tellus*, **58A**, 236–253.
- Meyers, M. P., R. L. Walko, J. Y. Harrington, and W. R. Cotton, 1997: New RAMS cloud microphysics parameterization. Part II: The two-moment scheme. *Atmos. Res.*, **45**, 3–39.
- Mlawer, E. J., S. J. Taubman, P. D. Brown, M. J. Iacono, and S. A. Clough, 1997: Radiative transfer for inhomogeneous atmosphere: RRTM, a validated correlated-k model for the longwave. *J. Geophys. Res.*, **102** (D14), 16 663–16 682.
- Morrison, H., and J. O. Pinto, 2006: Intercomparison of bulk cloud microphysics schemes in mesoscale simulations of springtime Arctic mixed-phase stratiform clouds. *Mon. Wea. Rev.*, **134**, 1880–1900.
- , J. A. Curry, and V. I. Khvorostyanov, 2005: A new double-moment microphysics parameterization for application in cloud

- and climate models. Part I: Description. *J. Atmos. Sci.*, **62**, 1665–1677.
- , G. Thompson, and V. Tatarkii, 2009: Impact of cloud microphysics on the development of trailing stratiform precipitation in a simulated squall line: Comparison of one- and two-moment schemes. *Mon. Wea. Rev.*, **137**, 991–1007.
- Murakami, M., T. Matsuc, H. Mizuno, and Y. Yamada, 1994: Mesoscale and microscale structures of snow clouds over the Sea of Japan. Part I: Evolution of microphysical structures in short-lived convective snow clouds. *J. Meteor. Soc. Japan*, **72**, 671–694.
- , Y. Yamada, T. Matsu, K. Iwanami, J. D. Marwitz, and G. Gordon, 2003: The precipitation process in convective cells embedded in deep snow bands over the Sea of Japan. *J. Meteor. Soc. Japan*, **81**, 515–531.
- Nielsen, N., 1997: An early-autumn polar low formation over the Norwegian Sea. *J. Geophys. Res.*, **102**, 13 955–13 973.
- Petty, G. W., 1994: Physical retrievals of over-ocean rain rate from multichannel microwave imagery. Part I: Theoretical characteristics of normalized polarization and scattering indices. *Meteor. Atmos. Phys.*, **54**, 79–100.
- , 1997: An intercomparison of oceanic precipitation frequencies from 10 SSM/I rain rate algorithms and shipboard present-weather reports. *J. Geophys. Res.*, **102**, 1757–1777.
- Rasmussen, E. A., and J. Turner, 2003: *Polar Lows: Mesoscale Weather Systems in the Polar Regions*. Cambridge University Press, 612 pp.
- Reisner, J. R., R. M. Rasmussen, and R. T. Bruintjes, 1998: Explicit forecasting of supercooled liquid water in winter storms using the MM5 mesoscale model. *Quart. J. Roy. Meteor. Soc.*, **124**, 1071–1107.
- Rutledge, S. A., and P. V. Hobbs, 1983: The mesoscale and microscale structure and organization of clouds and precipitation in midlatitude cyclones. VIII: A model for the “seeder-feeder” process in warm-frontal rainbands. *J. Atmos. Sci.*, **40**, 1185–1206.
- , and —, 1984: The mesoscale and microscale structure and organization of clouds and precipitation in midlatitude cyclones. XII: A diagnostic modeling study of precipitation development in narrow cloud-frontal rainbands. *J. Atmos. Sci.*, **41**, 2949–2972.
- Skamarock, W. C., and Coauthors, 2008: A description of the advanced research WRF version 3. NCAR/TN-468+STR, 126 pp.
- Tao, W.-K., and J. Simpson, 1993: The Goddard cumulus ensemble model. Part I: Model description. *Terr. Atmos. Oceanic Sci.*, **4**, 35–72.
- , —, and M. McCumber, 1989: An ice-water saturation adjustment. *Mon. Wea. Rev.*, **117**, 231–235.
- , and Coauthors, 2003: Microphysics, radiation and surface processes in the Goddard Cumulus Ensemble (GCE) model. *Meteor. Atmos. Phys.*, **82**, 97–137.
- Thompson, G., R. M. Rasmussen, and K. Manning, 2004: Explicit forecasts of winter precipitation using an improved bulk microphysics scheme. Part I: Description and sensitivity analysis. *Mon. Wea. Rev.*, **132**, 519–542.
- , P. R. Field, R. M. Rasmussen, and W. D. Hall, 2008: Explicit forecasts of winter precipitation using an improved bulk microphysics scheme. Part II: Implementation of a new snow parameterization. *Mon. Wea. Rev.*, **136**, 5095–5115.
- Wentz, F. J., and T. Meissner, 2007: Algorithm theoretical basis document: AMSR-E ocean algorithms supplement 1. Remote Sensing Systems, Santa Rosa, CA, 6 pp.
- Yanase, W., G. Fu, H. Niino, and T. Kato, 2004: A polar low over the Japan Sea on 21 January 1997. Part II: A numerical study. *Mon. Wea. Rev.*, **132**, 1552–1574.
- Ziegler, C. L., 1985: Retrieval of thermal and microphysical variables in observed convective storms. Part I: Model development and preliminary testing. *J. Atmos. Sci.*, **42**, 1487–1509.